



# Optimizing Interface Conductivity in Electronics



The latest eBook from  
**Advanced Optical Metrology.**  
Download for free.

Surface roughness is a key parameter for judging the performance of a given material's surface quality for its electronic application. A powerful tool to measure surface roughness is 3D laser scanning confocal microscopy (LSM), which will allow you to assess roughness and compare production and finishing methods, and improve these methods based on mathematical models.

Focus on creating high-conductivity electronic devices with minimal power loss using laser scanning microscopy is an effective tool to discern a variety of roughness parameters.

**EVIDENT**  
**OLYMPUS**

**WILEY**

# Smart and Multifunctional Fiber-Reinforced Composites of 2D Heterostructure-Based Textiles

Marzia Dulal, Md Rashedul Islam, Saptarshi Maiti, Mohammad Hamidul Islam, Iftikhar Ali, Amr M. Abdelkader, Kostya S. Novoselov, Shaila Afroj,\* and Nazmul Karim\*

Smart and multifunctional fiber reinforced polymer (FRP) composites with energy storage, sensing, and heating capabilities have gained significant interest for automotive, civil, and aerospace applications. However, achieving smart and multifunctional capabilities in an FRP composite while maintaining desired mechanical properties remains challenging. Here, a novel approach for layer-by-layer (LBL) deposition of 2D material (graphene and molybdenum disulfide, MoS<sub>2</sub>)-based heterostructure onto glass fiber fabric using a highly scalable manufacturing technique at a remarkable speed of  $\approx 150 \text{ m min}^{-1}$  is reported. This process enables the creation of smart textiles with integrated energy storage, sensing, and heating functionalities. This methodology combines gel-based electrolyte with a vacuum resin infusion technique, resulting in an efficient and stable smart FRP composite with an areal capacitance of up to  $\approx 182 \mu\text{F cm}^{-2}$  at  $10 \text{ mV s}^{-1}$ . The composite exhibits exceptional cyclic stability, maintaining  $\approx 90\%$  capacitance after 1000 cycles. Moreover, the smart composite demonstrates joule heating, reaching from  $\approx 24$  to  $\approx 27 \text{ }^\circ\text{C}$  within 120 s at 25 V. Additionally, the smart composite displays strain sensitivity by altering electrical resistance with longitudinal strain, enabling structural health monitoring. These findings highlight the potential of smart composites for multifunctional applications and provide an important step toward realizing their actual real-world applications.

response to environmental stimuli, such as mechanical, chemical, electrical, light, temperature, and moisture.<sup>[1]</sup> Such composites, composed of a polymer matrix reinforced with fibers and functional materials, have diverse applications in fields such as chemical and strain sensing, energy harvesting and storage, actuators, switches, robots, artificial muscles, and controlled drug delivery.<sup>[2]</sup> With the increasing demand for multifunctional materials in various industries,<sup>[3]</sup> there has been a growing interest in developing smart composites<sup>[4,5]</sup> that can perform multiple functions within a single structure. However, the development of smart composites presents several challenges, including achieving a balanced trade-off between the mechanical, electrical, and thermal properties of the composite material, and ensuring the compatibility of the individual components. Additionally, scalability and cost-effectiveness are important considerations in the development of smart composites.<sup>[6]</sup> Furthermore, metals, polymers, and carbon-based nanomaterials have traditionally been used to create smart composites.<sup>[7-9]</sup> However,


such materials are prone to oxidation, often have poor mechanical properties, and require complicated and expensive synthesis processes.<sup>[10,11]</sup> Among the various materials being explored for smart composite applications, two-dimensional (2D)

## 1. Introduction

Smart fiber-reinforced polymer (FRP) composites are a class of materials that exhibit reversible changes in their properties in

M. Dulal, M. R. Islam, M. H. Islam, I. Ali, S. Afroj, N. Karim  
Centre for Print Research  
The University of the West of England  
Bristol BS16 1QY, UK  
E-mail: shaila.afroj@uwe.ac.uk; nazmul.karim@uwe.ac.uk

S. Maiti  
Department of Fibres and Textile Processing Technology  
Institute of Chemical Technology  
Matunga (E), Mumbai 400019, India

 The ORCID identification number(s) for the author(s) of this article can be found under <https://doi.org/10.1002/adfm.202305901>

© 2023 The Authors. Advanced Functional Materials published by Wiley-VCH GmbH. This is an open access article under the terms of the Creative Commons Attribution License, which permits use, distribution and reproduction in any medium, provided the original work is properly cited.

DOI: 10.1002/adfm.202305901

A. M. Abdelkader  
Department of Design and Engineering  
Bournemouth University  
Talbot Campus, Poole BH12 5BB, UK

K. S. Novoselov  
Institute for Functional Intelligent Materials  
Department of Materials Science and Engineering  
National University of Singapore  
Singapore 117575, Singapore

K. S. Novoselov, S. Afroj, N. Karim  
National Graphene Institute (NGI)  
The University of Manchester  
Oxford Road, Manchester M13 9PL, UK



materials have shown promise due to their excellent mechanical, electrical, and thermal properties. In addition, such materials can be stacked together in LBL fashion to create heterostructures-based multifunctional composites with pre-designed properties and functionalities.

The concept of creating on-demand, designer materials is a fascinating idea, though it remains challenging to implement. It is difficult to achieve the optimal combination of various ingredients to create the ultimate material. Since the isolation of graphene in 2004, 2D materials have opened exciting opportunities to create heterostructures with diverse and tunable properties.<sup>[12]</sup> Such one-atom-thick crystals, including graphene, metals like niobium diselenide (NbSe<sub>2</sub>), semiconductors such as MoS<sub>2</sub>, and insulators like hexagonal boron nitride (hBN), have a broad range of stable properties.<sup>[13]</sup> By stacking different 2D crystals held together via van der Waals forces, we can create heterostructures with a far greater range of combinations than traditional growth methods. Nonetheless, there remains a need for a comprehensive strategy to address the challenge of blending crystals with distinct properties and generating highly scalable combinations with predetermined attributes and functionalities.

Graphene is by far the most extensively investigated 2D material due to its excellent mechanical, chemical, and electronic properties.<sup>[14–24]</sup> Graphene's distinctive physicochemical properties make it a promising candidate<sup>[25]</sup> material for supercapacitors,<sup>[22,26]</sup> electrochemical biosensors,<sup>[27,28]</sup> and physical sensors.<sup>[14,29,30]</sup> Additionally, other 2D materials (e.g., MoS<sub>2</sub>, hBN) received huge attention not only because of their 2D structure, but also due to their unique chemical and physical properties.<sup>[31–33]</sup> Depending on its crystalline phase, MoS<sub>2</sub>'s electronic properties can range from semiconductor to metallic. MoS<sub>2</sub> has a large bandgap that ranges from 1.2 (bulk material) to 1.8 eV (monolayer), making it a promising candidate material in nanoelectronics for high-performance and low-power device applications.<sup>[34]</sup> As graphene and MoS<sub>2</sub> have complementary properties<sup>[35]</sup> such as optical absorption, thermal conductivity, electronic band, and mechanical properties, it was reported that the combination of graphene and MoS<sub>2</sub> in specific ways to develop 2D heterostructures could potentially offer unique properties for various applications.<sup>[36–40]</sup> 2D heterostructures must be efficiently built in addition to having the necessary stability, reliability, pattern ability, and interface properties for the manufacture of smart devices.<sup>[41,42]</sup> Applications in graphene/MoS<sub>2</sub> heterostructures are severely hindered by the challenges of manufacturing van der Waals stacks of atomically thin materials on a large scale,<sup>[43]</sup> limited detectivity, ultra-weak light absorption.<sup>[44,45]</sup> Since graphene/MoS<sub>2</sub> devices are primarily created through mechanical exfoliation, their performance is severely constrained, limiting applications, and making them highly challenging to deploy in practical use. Therefore, there remains a need for ultrafast, low cost, and mass production of 2D heterostructure-based smart FRP for real-life multifunctional applications.

Here, our approach is to introduce the integration of 2D materials into composites and opens up new avenues for the development of high-performance smart materials for various applications. We report the ultrafast fabrication of smart FRP composites using a 2D heterostructure-based device as a functional material. We demonstrate the successful integration of a

graphene/MoS<sub>2</sub> heterostructure on the glass fabrics, and then infused such fabrics into a polymer matrix, resulting in a smart FRP composite with excellent mechanical properties and multifunctionalities. We then demonstrate potential multimodal uses of developed smart FRP composites for structural energy storage, joule surface heating, and health monitoring applications.

## 2. Results and Discussion

### 2.1. Design Approach

Multifunctional smart composite by design is an appealing concept that is extremely challenging to implement in reality. We currently lack a universal solution for the challenge of combining the best qualities of various components into one ideal structure. Here, we attempt to create and research a structure that can perform multiple functions (**Figure 1**). Our multifunctional smart composite includes the functionalities of structural energy storage, joule heating, and strain sensitivity. Initially, we investigated the functionality of 2D heterostructure-based glass fiber fabric as supercapacitor electrodes, heating textiles, and strain sensor. To replicate all these functionalities in a single composite structure, we integrated the 2D heterostructure-based glass fiber fabric in a composite structure as reinforcement materials, utilizing bio-epoxy resin as matrix and electrolyte coated glass fiber fabric as separator. We incorporated 2D heterostructures made of graphene/MoS<sub>2</sub> as their building blocks in glass fiber fabric because they have intriguing electronic properties at their nanoscale interfacial regions. This gives them the ability to control the confinement and transport of charge carriers, excitons, photons, phonons, and other particles in order to produce a wide range of exceptional physical, chemical, thermal, and/or mechanical properties. The electrochemical properties for advanced energy storage devices and electrocatalysis can be well controlled to meet some functionalities by logical design and synthesis of this heterostructures in our composite.<sup>[13,46]</sup> Additionally, a piezoresistive sensor network formation can perform continuous load monitoring<sup>[47]</sup> as a result of the integration of 2D heterostructure into FRP composite materials, which represents a smart structural solution. We then successfully demonstrated the functionality of our manufactured composite as structural energy storage device, heating element, and strain sensor, for the potential applications of structural battery, de-icing, and structural health monitoring (SHM) from a single structure, respectively (**Figure 1a,b**).

### 2.2. Scalable Production of Graphene/MoS<sub>2</sub> Heterostructure on Glass Fiber Fabrics

Here, we report a highly scalable method<sup>[48,49]</sup> for the LBL deposition of graphene/MoS<sub>2</sub> heterostructures onto glass fiber fabric. To the best of our knowledge, this is the first time such a technique has been applied to the manufacturing of next-generation smart composites for structural energy storage, surface joule heating, and SHM applications. We have used a laboratory-scale pad-dry-cure machine for the LBL deposition of 2D materials (graphene and MoS<sub>2</sub>) onto glass fabrics, enabling the creation of 2D heterostructures for smart FRP composites applications.

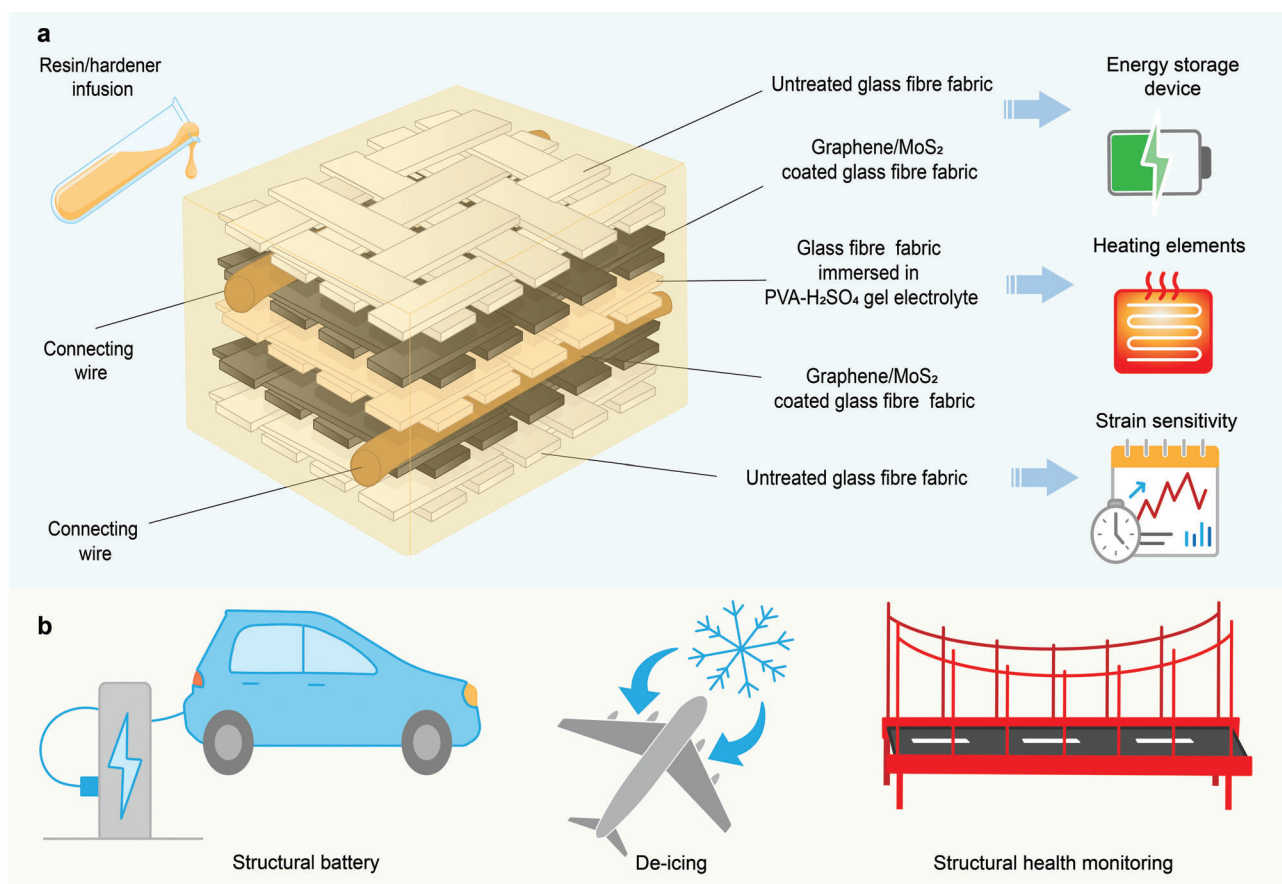


**Figure 1.** a) Design approach for 2D heterostructure-based smart and multifunctional composite and b) their potential applications.

Pad-dry-cure is a popular method for applying functional finishes (e.g., softening effect, antimicrobial, and water repellent) to textiles, and it is also an ultrafast continuous production method that can potentially coat up to  $\approx 150$  m of textiles in just 1 min. The schematic diagram for the pad-dry-cure method is shown in **Figure 2a**, where graphene and  $\text{MoS}_2$  are deposited onto control glass fiber fabric. **Figure 2b** displays the resulting sample after pad-dry-cure process. The presence of graphene flakes on the glass fiber is further demonstrated by scanning electron microscope (SEM) images. Untreated glass fiber can be seen as smooth fiber (**Figure 2c**). Significant flake deposition on individual fiber surfaces was seen after coating with graphene ink in graphene/ $\text{MoS}_2$  heterostructure (G3M1G3). A continuous conductive fabric is created by wrapping the individual fiber with flakes, as shown in **Figure 2d**, allowing current to flow through the structure.

The results presented in **Figure 2e** demonstrate a clear correlation between the number of graphene layers and the resistance of the 2D heterostructure. As the number of graphene layers increases, the resistance decreases, with an average resistance of  $\approx 0.48 \text{ k}\Omega \text{ cm}^{-1}$  for up to six graphene layers. Additionally, we observed that the add-on% increases rapidly until the third layer of graphene deposition but then increases slowly until the sixth layer, with the add-on% moving averages remaining relatively constant after that point. Interestingly, the add-on% of the resultant G3M1G3 structure (three layers of graphene, one layer of

$\text{MoS}_2$ , three layers of graphene) was  $\approx 26.56\%$  when we added another layer of  $\text{MoS}_2$  in the middle of the six graphene layers, meaning three graphene layers, one  $\text{MoS}_2$  layer, and again three graphene layers were deposited in this sequence. This is  $\approx 42\%$  better than the resultant G6 add-on%, which as we had previously observed, was  $\approx 18.68\%$ . Later analysis and experiments, however, showed that the add-on% does not change that much ( $\approx 26\%$ ) even when the number of  $\text{MoS}_2$  layer deposition was increased from one to three in the graphene/ $\text{MoS}_2$  heterostructure. Instead, we found that the resistance increased with the increase  $\text{MoS}_2$  layer deposition in the middle from one to three in graphene/ $\text{MoS}_2$  heterostructure because when interlayer distance increases, the interlayer connection weakens and the charge transfer from the graphene layer to the  $\text{MoS}_2$  layer is less,<sup>[50]</sup> which led us to choose a single deposited  $\text{MoS}_2$  layer in the resulting graphene/ $\text{MoS}_2$  heterostructure (G3M1G3) for further testing and characterization.

### 2.3. Graphene/ $\text{MoS}_2$ Heterostructure-Based Energy Storage Device

Graphene/ $\text{MoS}_2$  hybrid-coated textiles have the potential to serve as ideal candidate electrodes for energy storage devices due to their high conductivity and mechanical flexibility within the interlayer distance of graphene/ $\text{MoS}_2$ .<sup>[50,51]</sup> The combination of

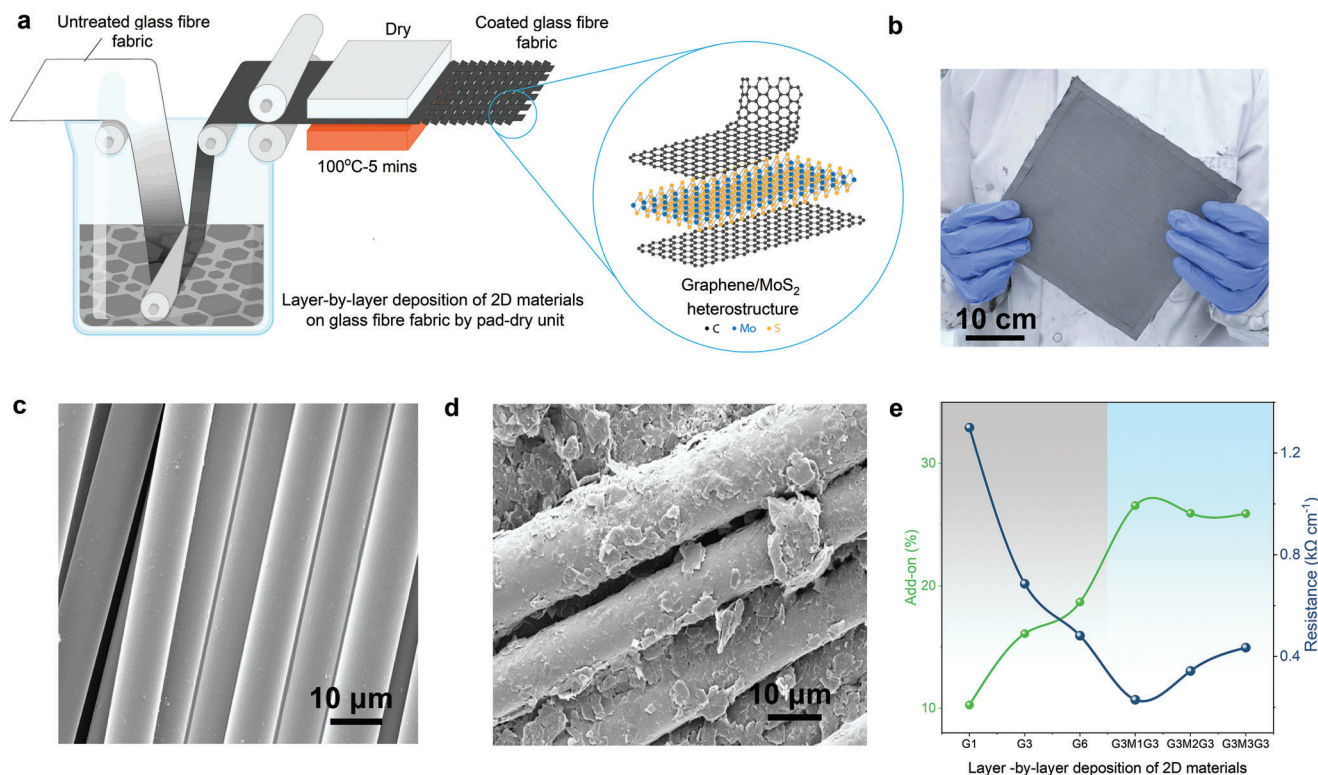


**Figure 2.** a) LBL deposition of graphene and MoS<sub>2</sub> for the creation of 2D heterostructure on glass fiber fabrics via highly scalable pad-dry-cure process; b) 2D heterostructure coated glass fiber fabric; c) SEM image of smooth and featureless control glass fiber fabric (×3000); d) SEM image of 2D heterostructure-based glass fiber fabrics (G3M1G3) (×3000); e) The effect of LBL deposition of 2D materials on the add-on.% and resistance (kΩ cm<sup>-1</sup>) of 2D heterostructure-based glass fiber fabrics.

graphene and MoS<sub>2</sub> flakes on the textiles creates a porous film with nano- and micro-channels, resulting from the wide range in size and thickness.<sup>[52,53]</sup> Such unique structure facilitates the interaction between the electrolyte and the graphene/MoS<sub>2</sub> hybrid coating, improving its wettability. The electrolyte's wettability is a critical factor in the development of high-performance energy storage devices since uneven wetting can lead to an unstable solid electrolyte interface film and an uneven distribution of current density.<sup>[54]</sup> Energy storage devices use a range of mechanisms, such as electrical double-layer and pseudocapacitance, to achieve high specific capacitance. To create a high-performance energy storage device such as a supercapacitor, two methods can be employed.<sup>[55]</sup> The first method involves increasing the surface area to boost the capacitance of the double layer (Figure 3a), while the second method aims to raise the likelihood of reversible faradic redox reactions to increase the capacitance of the pseudocapacitor (Figure 3b). To improve the capacitive properties of the energy storage device, we intend to construct a heterostructure by combining two types of 2D materials, graphene and MoS<sub>2</sub>, which exhibit double-layer-type and pseudocapacitor-type capacitance, respectively.

To demonstrate the feasibility of using LBL-based electrodes in energy storage devices, we constructed each device with two identical coated electrodes and a poly(vinyl alcohol) (PVA)-H<sub>2</sub>SO<sub>4</sub> gel electrolyte, as shown in Figure 3c. Copper wires were used as current collectors and were connected directly to the potentiostat terminals. Cyclic voltammetry (CV) and galvanostatic

charge–discharge (GCD) were used to evaluate the electrochemical performance of the sandwich-shaped symmetric energy storage device. Our results indicate that increasing the number of graphene layers in the electrode improves the areal capacitance performance up to six layers (G6), as shown in Figure 3d. However, the addition of one layer of MoS<sub>2</sub> to configure a three graphene, one MoS<sub>2</sub>, and three graphene layers (i.e., G3M1G3) results in the highest areal capacitance. However, further increase in the number of MoS<sub>2</sub> layers in this graphene heterostructure by more than one-layer leads to a decrease in areal capacitance, as shown in Figure 3d. Initially, the inclusion of a single coating layer of MoS<sub>2</sub> serves to fill defects and voids on the graphene surface, thereby creating additional active sites for charge transfer and enhancing the overall conductivity of the fabric. Consequently, this leads to an increase in the areal capacitance. However, as the number of MoS<sub>2</sub> layers is further increased, it begins to impede conductivity, as indicated by resistance changes shown in Figure 2e. This can be attributed to the insulating nature of MoS<sub>2</sub>, which, with a higher number of layers, hinders the material's charge transfer pathways. The influence of this effect is evident in Figure 3d, where the hybrid G3M1G3 sample demonstrates an areal capacitance of ≈18.76 mF cm<sup>-2</sup> at a scan rate of 10 mV s<sup>-1</sup>, while the G6-based supercapacitor exhibits a slightly lower capacitance of around 14.90 mF cm<sup>-2</sup>.

It has been reported that increasing the scan rate can cause a decrease in capacitance due to ion transport limitations near the electrodes.<sup>[57,58]</sup> Figure 3e depicts CV curves for the



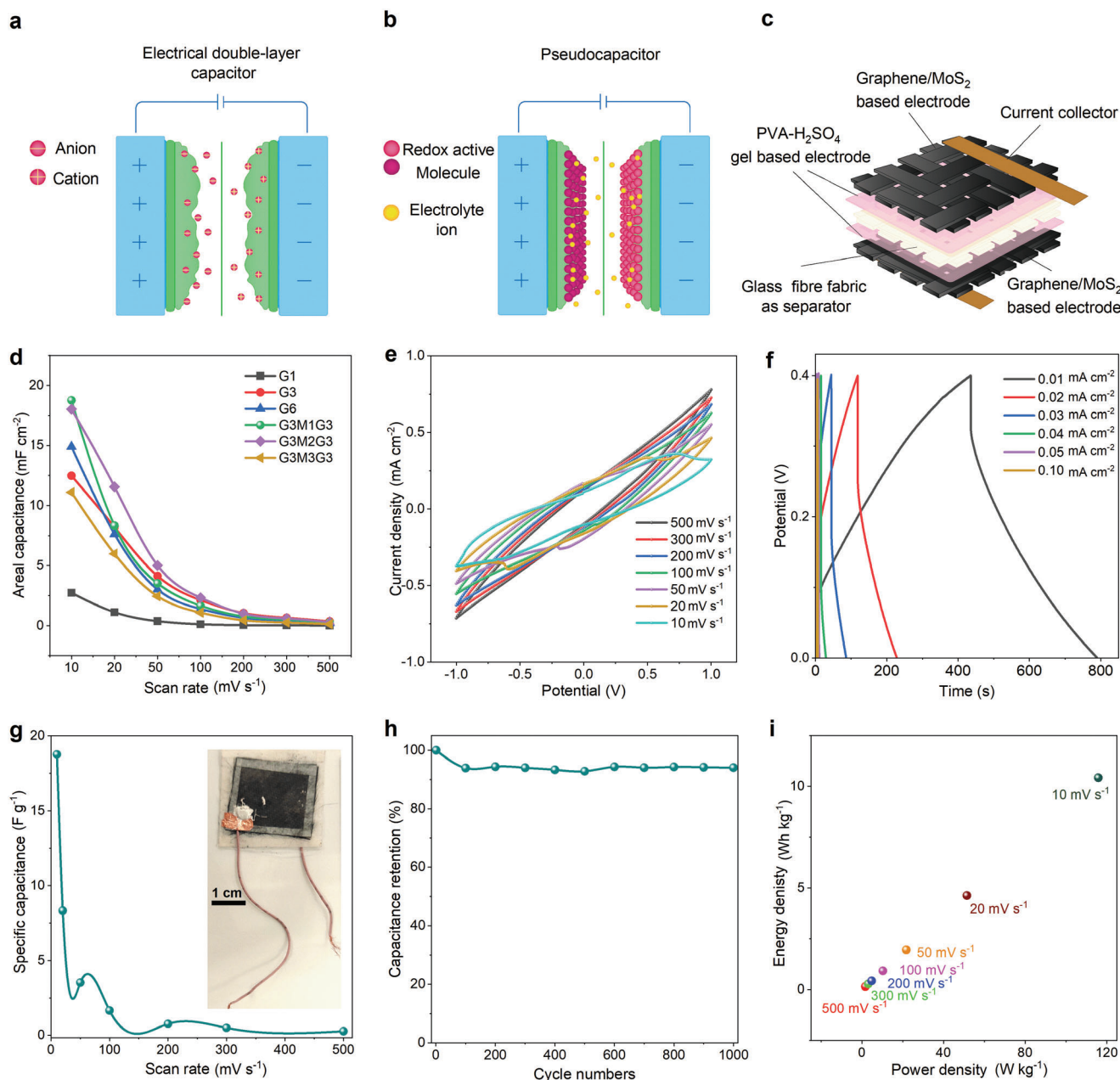


**Figure 3.** The schematic diagram of a) an EDLC and b) a redox type of pseudocapacitor;<sup>[56]</sup> c) Schematic diagram of graphene/MoS<sub>2</sub> heterostructure-based energy storage device; d) Areal capacitance of G1, G3, G6, G3M1G3, G3M2G3, and G3M3G3-based energy storage devices at different scan rates; e) CV graph of G3M1G3 based energy storage device at different scan rates; f) GCD graph of G3M1G3 based energy storage device at different current density; g) Specific Capacitance of G3M1G3 based energy storage device at different scan rates; h) Changes of capacitance retention (%) of the G3M1G3 based energy storage device at different cycles; i) Changes of energy density with the change of power density due to different scan rates.

supercapacitor device made of G3M1G3 coated electrodes at various scan rates. CV measurements were performed in a potential window (V) between  $-1.0$  and  $1.0$  V. The curves possess a large, enveloped area even at high scan rates, resulting from the excellent double layer capacitance of graphene and high pseudocapacitance of MoS<sub>2</sub>. Moreover, in order to fully grasp the differences, we additionally assess various CV graphs of G1, G3, G6, G3M2G3, and G3M3G3 coated glass fiber fabric electrodes for energy storage devices to compare with G3M1G3, which is

shown in Figure S1a, Supporting Information. For the galvanostatic charging/discharging test of the as-prepared supercapacitor, a current density of  $0.01$  to  $0.1$  mA cm<sup>-2</sup> was used, as shown in Figure 3f. The G3M1G3-based energy storage device has the longest discharging time ( $t$ ) at a current density of  $0.01$  mA cm<sup>-2</sup>, which is  $\approx 354.5$  s ( $0.09$  h) in the potential range of  $0$  to  $0.4$  V. It is worth noting that the maximum current that can be applied in a GCD experiment is limited by the ability of the system to maintain the triangular shape without causing a significant voltage

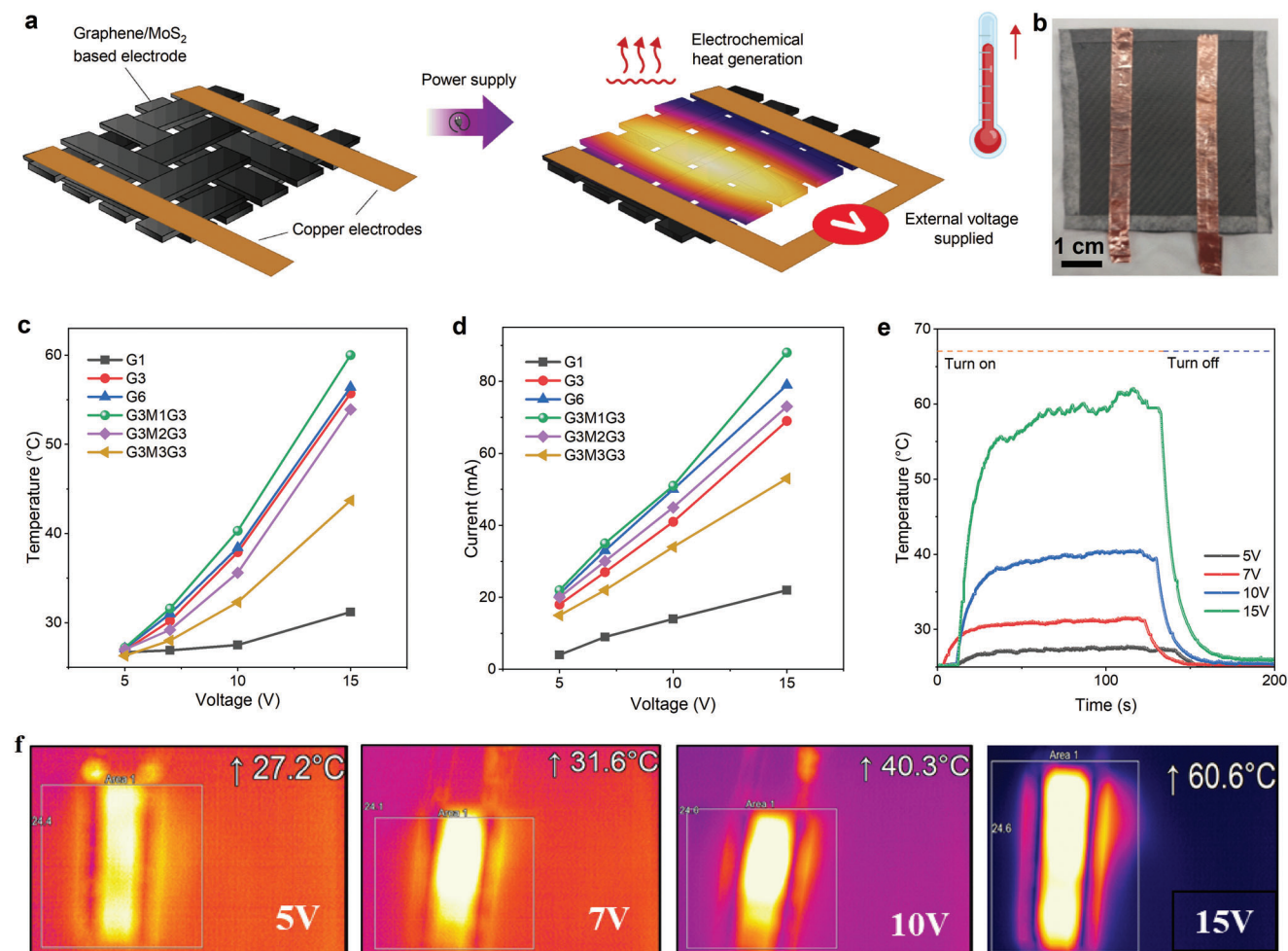


**Figure 4.** a) Schematic diagram of heating elements; b) Original sample of heating elements; c) Temperature change of G1, G3, G6, G3M1G3, G3M2G3, and G3M3G3-based heating elements with the change of supplied voltage 5, 7, 10, and 15 V; d) *I*-*V* graphs of G1, G3, G6, G3M1G3, G3M2G3, and G3M3G3-based heating elements with the change of supplied voltage 5, 7, 10, and 15 V; e) Time-Temperature graphs of G3M1G3-based heating element at different supplied voltages with the influence of heat turns on and turn-off; f) Surface temperature's thermal images of G3M1G3-based heating element at different supplied voltages.

drop when the current polarity is switched. Similarly, the maximum voltage that can be applied to GCD analysis is one that keeps both the charging and discharging branches of the GCD linear.

In order to improve the performance of similar devices, researchers have investigated heterostructures of 2D materials, including derivatives of graphene and MoS<sub>2</sub>, to enhance the performance of supercapacitors.<sup>[59–65]</sup> However, such studies have not been conducted with the goal of developing energy storage devices for textiles and their composites. Our work focuses on demonstrating the energy storage capability of textiles. Despite being a relatively new field, our textile-based energy storage device, which utilizes LBL deposition of graphene/MoS<sub>2</sub> and a PVA-H<sub>2</sub>SO<sub>4</sub> gel electrolyte, represents a promising starting point. We have shown that this device has a specific capacitance of  $\approx 18.7 \text{ F g}^{-1}$  (Figure 3g) and a capacitance retention of  $\approx 94\%$  even after 1000 cycles (Figure 3h). In addition, such supercapacitor is capable of delivering an energy density of  $\approx 10.42 \text{ Wh kg}^{-1}$  at a power density of  $\approx 115.82 \text{ W kg}^{-1}$  (Figure 3i).

#### 2.4. Graphene/MoS<sub>2</sub> Heterostructure-Based Fabric for Joule Heating

Joule heating is a physical phenomenon that occurs when a current flows through an electrical conductor, resulting in the production of thermal energy.<sup>[66]</sup> This thermal energy causes an increase in the temperature of the conductor material, leading to the term “heating.” Joule heating is essentially a conversion of “electrical energy” into “thermal energy,” in accordance with the principle of energy conservation. The application of joule heating to fibers, textiles, and woven fabrics made of conductive materials has gained popularity in the fields of heating elements for composites and therapeutic purposes. When conductive fibers and textiles are connected to external electrodes, illustrated in Figure 4a, electrical currents and resistance cause joule heating. This heating effect can be utilized to provide stable, controlled thermal regulation to textiles, often requiring lower power sources.<sup>[67,68]</sup> To practically implement active heating textiles, the surface of the textile material is coated LBL with

2D materials. The morphology, electrical conductivities, and thermal conductivities of epoxy-based composites,<sup>[69]</sup> as well as the surface heater,<sup>[70]</sup> are linked to joule heating performance. In our study, we explored the use of various configurations of graphene and MoS<sub>2</sub> heterostructure layers to create conductive heating textiles. Figure 4b shows an image of the glass fiber fabric coated with such 2D materials. Joule heating also provides a direct path for inside-out crystallization of the conformal MoS<sub>2</sub> layer, enabling excellent interfacial interaction between the MoS<sub>2</sub> and the underlying carbon-based material (e.g., 2D graphene).<sup>[71]</sup> Due to extremely quick heating, simple processing, and ability to integrate with textiles<sup>[70]</sup> and other components,<sup>[72]</sup> in our study we investigated various configurations of graphene and MoS<sub>2</sub> heterostructure layers to create conductive heating textiles where glass fiber fabric was coated with these 2D materials (Figure 4b).

We conducted electro-thermal characterization using six different samples of coated glass fiber fabric, with five specimens for each category, all of the same area (4 cm × 4 cm). We applied various voltages (5, 7, 10, and 15 V) across the entire sample, and measured the change in temperature of the coated fabric (due to joule heating) (Figure 4c) and the current–voltage characteristics (Figure 4d). For instance, applying 15 V to the glass fiber fabric coated with six layers of graphene (G6) resulted in a current of ≈0.08 A and the temperature reaching up to ≈56.4 °C within 120 s. Figure 4c,d illustrates that the currents and temperatures exhibit an upward trend with an increasing number of graphene layers in the glass fiber fabric, aligning with Ohm's law, which establishes a direct relationship between current and applied voltage in a conductor. Graphene, known for its unique composition and characteristics, serves as an exceptional electrical conductor. Consequently, the fabric's overall conductivity improves as more graphene layers are integrated into its structure. Upon the application of a voltage, this enhanced conductivity facilitates a higher flow of electrical current, resulting in increased current values. As the current passes through the conductive fabric, it encounters resistance, leading to the generation of heat. By employing layers of G3M1G3-coated glass fiber fabric, the temperature of the structure reaches ≈60 °C within the same duration (120 s) and at the same voltage (15 V), with the current reaching 0.09A. This clearly demonstrates the superior performance compared to utilizing only G6 layers. Therefore, it becomes evident that an optimized MoS<sub>2</sub> layer can enhance joule heating in graphene-coated glass fiber fabric by filling the voids on the graphene surface, thereby promoting greater charge transfer mobility and improved overall conductivity. However, when the number of MoS<sub>2</sub> layers exceeds one, a decline in temperature and current is observed. This suggests that an increased number of insulating MoS<sub>2</sub> layers may introduce higher resistance, impede current flow, and result in reduced heat generation. The time-temperature curves of a glass fiber fabric with conductive G3M1G3 networks for an integrated joule heater for various voltages and temperature stability are shown in Figure 4e (Figure S1b, Supporting Information, compares G3M1G3 with the same time-temperature graph for G1, G3, G6, G3M2G3, and G3M3G3 coated glass fiber electrodes for heating elements). This textile framework can thus be considered for the use in surface heating applications. Thermal images (Figure 4f) show that heat is distributed uniformly across the area of the conductive coated glass fiber fabric.

## 2.5. Graphene/MoS<sub>2</sub> Heterostructure-Based Fabric for Strain Sensitivity

Strain sensors have greatly evolved in recent years and are now used in a wide variety of applications. However, despite the remarkable advancement in the development of nanomaterials, creating strain sensors in a scalable approach that enables high sensitivity and stability over a long period of time remains a challenge for potential applications in wearable electronics, soft robotics, and healthcare monitoring. In this study, we developed a strain sensor based on graphene/MoS<sub>2</sub> heterostructure by utilizing the high mobility of graphene and the structural rigidity of MoS<sub>2</sub>. To demonstrate the strain sensitivity, we used woven glass fiber with graphene/MoS<sub>2</sub> coatings, and at least five samples of each strain sensor were tested to investigate changes in relative resistance ( $\Delta R/R_0$ ). Piezoresistivity-based sensors typically rely on translating changes in resistance (Figure 5a), which typically follow a linear relationship, into external mechanical loading.<sup>[73]</sup> The gauge factor (GF) is the first metric used to measure the performance of such piezoresistive sensors, and it is defined as the relative resistance changes versus tensile strain.<sup>[74]</sup> A low GF or a nonlinear response can result in poor repeatability for strain/release cycles.<sup>[75]</sup> To analyze our G3M1G3 coated (Figure 5b) strain sensor's performance we calculated the GF using the expression

$$GF = \frac{\Delta R/R_0}{\epsilon} \quad (1)$$

where  $\Delta R = R_\epsilon - R_0$ ;  $R_0$  and  $R_\epsilon$  are the initial resistance and resistance at a specific strain  $\epsilon$ , respectively.

The load elongation graph in Figure 5c shows that treating the sample with G3M1G3 improves the load by around 8.62% while changing the strain by about 5%, compared to the untreated sample (Figure S1c, Supporting Information, compares G3M1G3 with the same load-elongation curve for G1, G3, G6, G3M2G3, and G3M3G3-based glass fiber fabric electrodes). Figure 5d demonstrates that  $\Delta R/R_0$  increases linearly with the strain under tensile load. Our graphene/MoS<sub>2</sub> heterostructure-based strain sensor exhibits a moderate gauge factor (GF) on glass fiber fabric, reaching ≈26.86 at a maximum strain of 5% (with  $\Delta R/R_0$  of ≈134.30%) (Figure 5d). This result aligns with the principle of strain sensor performance, wherein a high gauge factor signifies greater resistance change and increased sensitivity.<sup>[76,77]</sup> The load versus elongation curve for five cycles of cyclic tensile testing at 1% and 2% strains is depicted in Figure 5e. As strain% increases, the load and elongation also rise. Cyclic tensile testing was conducted for five cycles at 1% and 2% strain levels at the same speed. The graph shows that at 2% strain, the sample rises to an average load of ≈385 N before returning, whereas at 1% strain, the sample reaches an average load of 185 N before returning, and the load decreases slightly with each subsequent cycle.

Figure 5f indicates that during cyclic testing,  $\Delta R/R_0$  changes irreversibly under a given strain at the beginning, but after straining gets on the reversible path. We performed five cycles of 2% and 1% strain at various speeds (1 and 2 mm min<sup>-1</sup>) and ran 100 cycles at 1 mm min<sup>-1</sup> and 1% strain to observe the cyclic stability. Figure 5g illustrates that the relative  $\Delta R/R_0$  changes gradually with no radical shift after 6000s (30 cycles). The sensor can



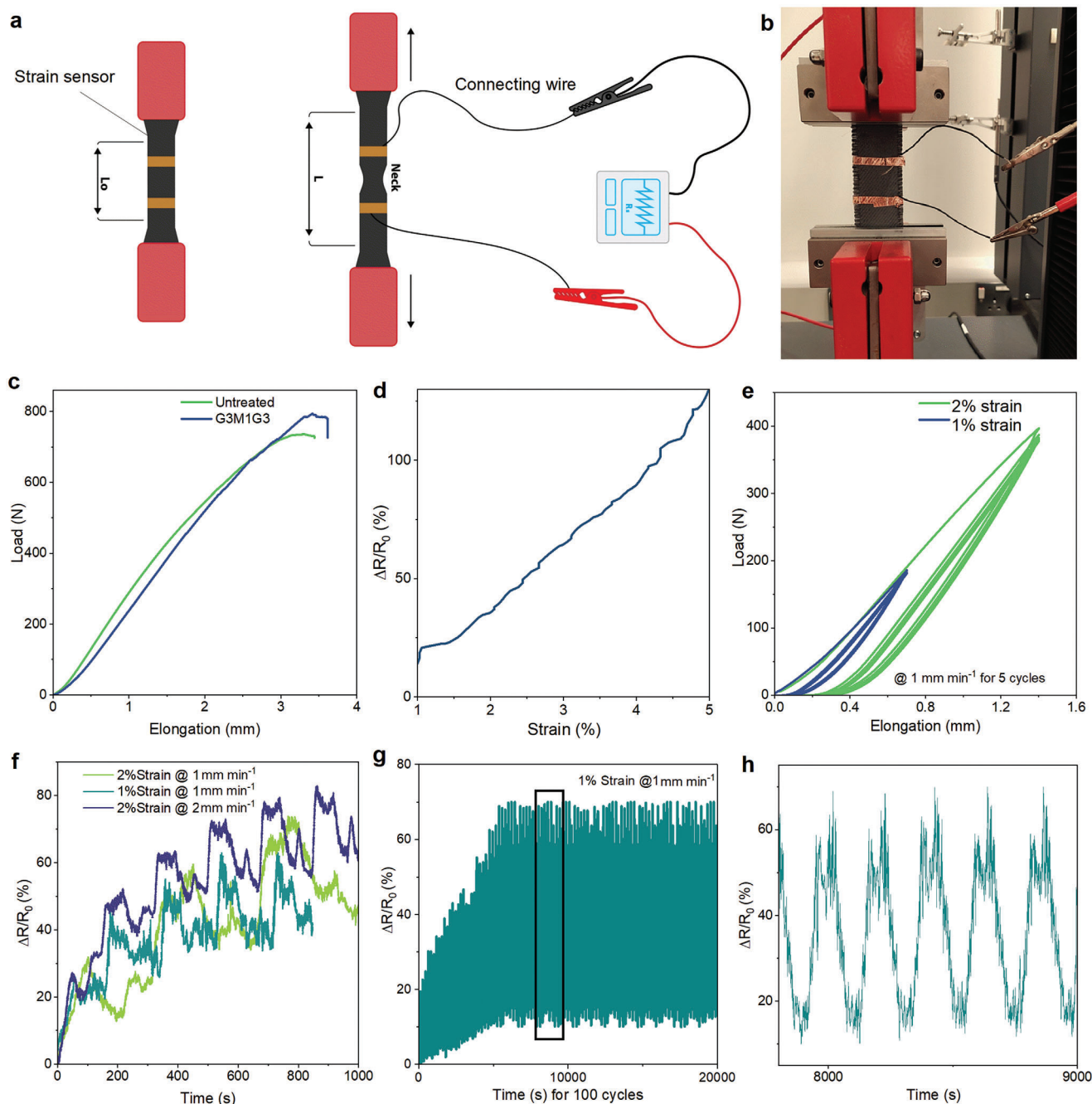


**Figure 5.** a) Schematic diagram of strain sensitivity measurement; b) Original sample testing image; c) Load–elongation graph of tensile testing of untreated and graphene/MoS<sub>2</sub> heterostructure treated glass fiber fabric (G3M1G3); d)  $\Delta R/R_0$  changes with the strain; e) Load–elongation graph of cyclic tensile testing at 1 mm min<sup>-1</sup> speed up to 1% and 2% strain for five cycles; f)  $\Delta R/R_0$  change of cyclic tensile test for five cycles with time at different strain and same speed; g)  $\Delta R/R_0$  change of cyclic tensile test for 100 cycles with time up to 1% strain at 1 mm min<sup>-1</sup>; h) Selective area  $\Delta R/R_0$  change at wide angle for cyclic stability with time.

operate for at least 20 000 s (100 cycles) under a strain of 1%. Even after numerous stretching–releasing cycles, the sensor resistance can return to its initial state, with an average relative resistance change of 70%. Figure 5h provides a close-up of the curve between  $\approx 8000$  and  $\approx 9000$  s in Figure 5g, which presents the relative resistance changes–time curves of the G3M1G3 sensor.

## 2.6. Concurrent Characterization of Smart Composite Structure

In previous sections, we demonstrated that the deposition of 2D material-based heterostructures onto glass fiber fabric using the LBL technique resulted in multifunctional textiles with promising applications in energy storage, joule heating, and strain sensing. Our aim is to develop a smart and multifunctional FRP

composite by incorporating all these functions into a single composite and that can perform these functions concurrently when needed with potential applications in the automotive, civil, and aerospace industries. **Figure 6a** illustrates the manufacturing flow of the proposed smart composite, while **Figure 6b** shows the representation of the original sample. To develop smart composites for energy storage, we formed graphene/MoS<sub>2</sub> heterostructure-based composites using a vacuum assisted resin infusion process (VARI) technique and an acid-based electrolyte. These composites have relatively lower tensile properties but can be used for various applications in energy storage, joule heating, and strain sensing.

The electrochemical performance of the structural energy storage composite is presented in **Figure 6c**, where typical CV profiles are displayed at various scan rates. **Figure 6d** shows the areal capacitance of this composite at different scan rates, with the highest capacitance achieved being 0.18 mF cm<sup>-2</sup> (182 μF cm<sup>-2</sup>) at a scan rate of 10 mV s<sup>-1</sup>. Furthermore, we tested the cyclic stability of the structural energy storage device, as shown in **Figure 6e**, where our device exhibits excellent stability of 90% even after 1000 cycles.

We also investigated the joule heating characteristics of the developed multifunctional composite structure. **Figure 6f** shows the current–voltage (*I*–*V*) curve of the graphene/MoS<sub>2</sub> heterostructure-based (G3M1G3) composite, as well as the temperature rise. Although the temperature does not increase significantly as the voltage increases from 15 to 25 V, the current gradually changes from 8 to 12 mA linearly. It is evident from the time temperature graph (**Figure 6g**) that with an increase in applied voltage of up to 25 V, the temperature rose from ≈24 to ≈27 °C in just 120 s. However, the heat dissipated quickly when turned off, taking less than 100 s for the temperature to drop. **Figure 6h** displays the actual thermal images for the composite's surface temperature changes at 15, 20, and 25 V.

The stress–strain graph in **Figure 6i** shows that the untreated composite breaks (**Figures S2 and S3**, Supporting Information) when the stress reaches ≈391.09 MPa at strain ≈2.84%, but the G3M1G3 composite breaks before that threshold, which is ≈297.36 MPa at strain ≈3.25%. The interfacial bond between the fibers and the matrix, as well as the existence of void somehow may result in a reduction in stress. Despite a decrease in mechanical properties, the smart sensing capabilities of our developed composite can be highly beneficial for the creation of smart structures that can monitor their own stress levels. This is made possible by variations in the degree of fiber alignment, which causes the electrical resistance of the composite to change reversibly with longitudinal strain. Our smart composite structure (G3M1G3) also demonstrated excellent strain sensitivity, making it an effective strain sensing device. The composite's resistance changed in response to applied strains, and we measured the electrical conductivity and resistance three times to determine the average values. As shown in **Figure 6j**, as strain increases up to 0.5%, the Δ*R*/*R*<sub>0</sub> reaches ≈16%, and GF becomes ≈32.

From the cyclic test results shown in **Figure 6k**, we observed that the Δ*R*/*R*<sub>0</sub> value increased with each successive five cycles. This behavior is attributed to the fiber arrangement becoming less neat at the end of the first cycle, which causes a disturbance. The likelihood of adjacent fiber layers touching one another increases with a less orderly fiber arrangement. Previ-

ous studies have shown that multifunctional composites with an average tensile strength can yield better energy densities, and although our smart multifunctional composite shows lower strength compared to untreated composite, it still has better mechanical strength than some other composites.<sup>[80–83]</sup> Additionally, our composite demonstrates better sensitivity and a slight increase in capacitance, as well as improvements in heating elements using gel-based electrolytes in the graphene/MoS<sub>2</sub> heterostructure. Overall, these findings represent an initial proof of concept for our multifunctional composite material.

### 3. Conclusion

We have demonstrated the successful creation of smart FRP composites based on a graphene/MoS<sub>2</sub> heterostructure for multifunctional applications. These composites exhibit remarkable mechanical and electrochemical properties, including an areal capacitance of ≈182 μF cm<sup>-2</sup> and an elastic modulus of ≈8 GPa when used to create structural battery composite materials. The strain sensitivity of such composites, with a Δ*R*/*R*<sub>0</sub> rise of up to ≈16% when strain is up to ≈0.5% with slight surface heating upon increasing the applied voltage by up to 25 V, the temperature rose from ≈24 to ≈27 °C in ≈120 s, surpasses any previous structural battery materials reported in the literature (**Table S1**, Supporting Information). Overall, our findings provide important insights into the complementary, and occasionally antagonistic, mechanical, and electrochemical functions of graphene/MoS<sub>2</sub> heterostructures. Our results demonstrate the potential of using 2D material-based heterostructures to mitigate the negative mechanical properties of each constituent and create smart composites with improved mechanical and electrochemical properties. We hope that our work will inspire further research in this area and lead to the development of novel and high-performance smart composites for a variety of applications.

### 4. Experimental Section

**Materials:** The microfluidized graphene (≈7 nm thick, <2 μm lateral size, <30% wt%) and molybdenum disulfide (MoS<sub>2</sub>) (few layer <2 μm lateral size, 100 g L<sup>-1</sup>) dispersions were purchased from Cambridge Graphene Ltd (UK). PVA (molecular weight: 31 000–50 000, 98–99% hydrolyzed) and sulfuric acid (H<sub>2</sub>SO<sub>4</sub>) (puriss, 95–97%) were purchased from Merck, UK. ONE high biobased epoxy laminating resin (30% bio-content) and ONS high biobased slow laminating hardener (mixed bio-content 21%), based on Super Sap formulation were purchased from Entropy Resins, UK, and 200 GSM (grams per square meter) twill woven glass fabrics were purchased from Easy Composites, UK.

**LBL Deposition of 2D Materials into Glass fiber Fabric:** A simple laboratory scale pad–dry–cure method was used to coat glass fiber fabric with varying numbers of layers of graphene and MoS<sub>2</sub> using a BVHP PADDER—vertical and horizontal (350) 2 Bowl (Roaches, UK). The coated fabrics were then batch dried with a Mini Thermo Oven Type 350 Special (Roaches, UK) at 100 °C for 5 min. The padding roller pressure and speed were adjusted and the fabrics (25 cm × 25 cm) were periodically padded with 2D material dispersions in different layer configuration. Each padding cycle included one padding and one drying pass. Samples were repeatedly pad-dried as following which denoted the number of padding (coating) cycles. The curing time and temperature of the pad-dried samples were kept for 5 min at 100 °C in the oven as reported previously.<sup>[52]</sup>

- 1) One pass coating of glass fiber fabric with graphene ink—G 1

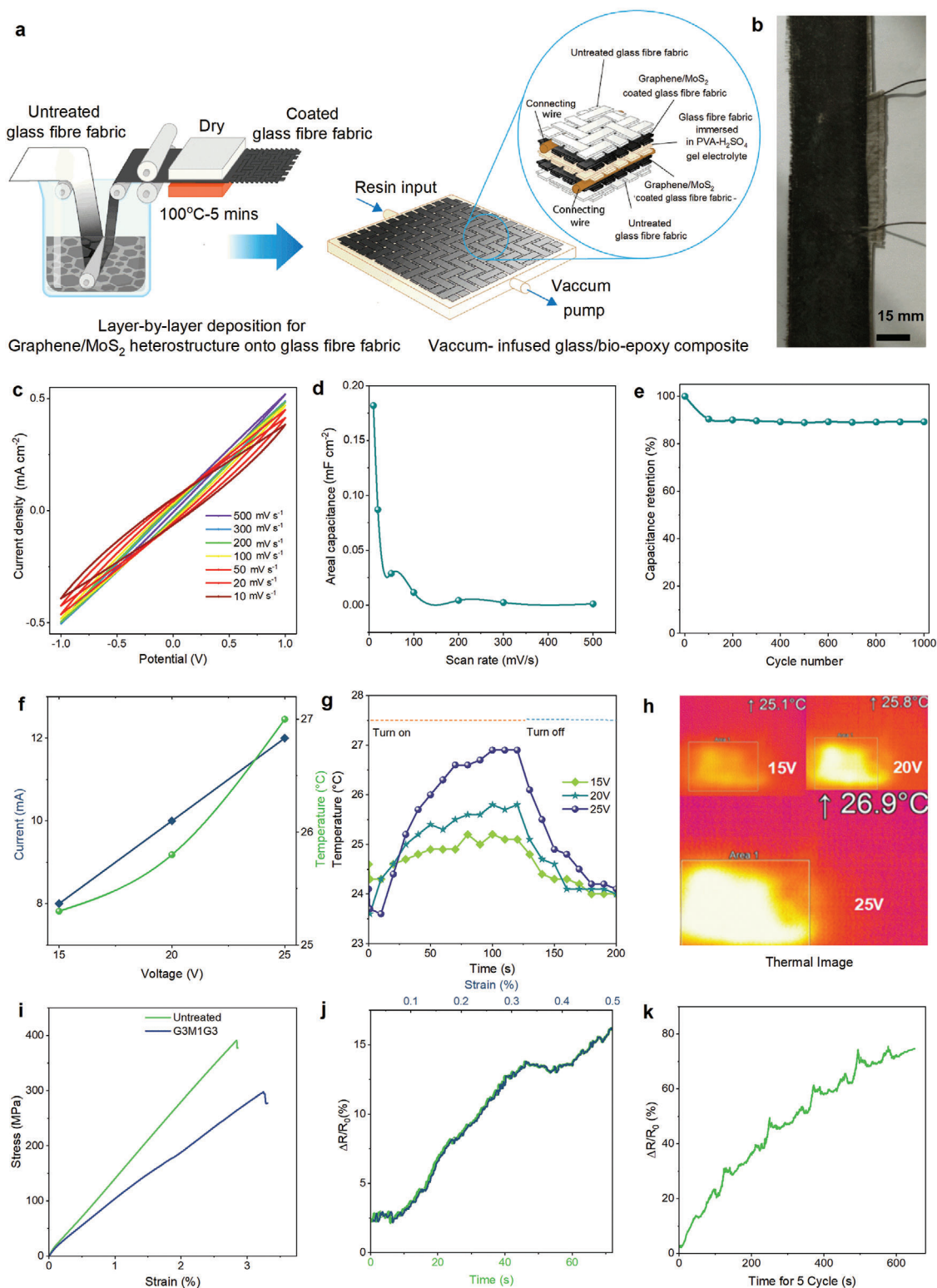


**Figure 6.** a) Schematic of smart composite manufacturing process<sup>[78–79]</sup> from untreated fabric pad-dry to vacuum infusion; b) Original sample of Smart composite; Structural energy storage device performance: c) CV graph, d) areal capacitance at different scan rates of smart composite, and e) capacitance retention (%) at different cycles; Joule heating performance: f) Current and temperature changes with the change of supplied voltages, g) time–temperature graph at different voltages with the influence of heat turn on and turn off, and h) thermal images of samples at different voltages; Strain sensitivity performance: i) Stress–strain Graph of untreated and G3M1G3-based composites, j)  $\Delta R/R_0$  change in comparison with time and strain, k) and  $\Delta R/R_0$  change with time for five cycles.



- 2) Three pass coating of glass fiber fabric with graphene ink—G3
- 3) Six pass coating of glass fiber fabric with graphene ink—G6
- 4) Three graphene—one MoS<sub>2</sub>—three graphene pass coating of glass fiber fabric —G3M1G3
- 5) Three graphene—two MoS<sub>2</sub>—three graphene pass coating of glass fiber fabric —G3M2G3
- 6) Three graphene—three MoS<sub>2</sub>—three graphene pass coating of glass fiber fabric —G3M3G3

The graphene and MoS<sub>2</sub> add-on (%) were calculated using following equation.

$$\text{Add-on (\%)} = \frac{m_n - m_0}{m_0} \times 100 \quad (2)$$

where  $m_0$  is the mass of the uncoated fabric specimen and  $m_n$  is the mass of “ $n$ ”-time graphene/MoS<sub>2</sub>-coated fabric specimen.

**Fabrication of Energy Storage Device:** The energy storage device was developed in the form of a sandwich, with the coated samples acting as electrode materials on the top and bottom layers and the middle separator, which was made of a piece of glass fiber fabric immersed in a hydrogel-polymer electrolyte PVA doped with H<sub>2</sub>SO<sub>4</sub> (Figure 3c).<sup>[84,85]</sup> Current was collected by connecting copper wires to the fabric surface using silver electronic paste DM-SIP-3067S (DYCOTEC Materials, UK). To ensure good electrical contact with the measuring workstation, copper wire was, however, permanently adhered to the ends of each electrode. The PVA-H<sub>2</sub>SO<sub>4</sub> gel electrolyte was made as following: After adding 1 g of PVA to 10 mL of deionized water, 1 g of H<sub>2</sub>SO<sub>4</sub> was added. Afterward, the entire mixture was heated to ≈85 °C while being stirred up until the solution was clear. The electrolyte was drop-casted onto the separator fabric and maintained in the aforementioned sandwiched form. It was then left to dry overnight under ambient conditions to ensure complete wetting of the electrode by the electrolyte and allow for the evaporation of any excess water.<sup>[18]</sup>

The electrochemical performances of the as-fabricated textile energy storage device were investigated by cyclic voltammetry (CV), and GCD tests. The electrochemical measurements were performed on an Iviumstat electrochemical interface. The CV and GCD measures were conducted in the potential range –1.0 to 1.0 V at different scan rates and current densities to calculate the following key metrics<sup>[86]</sup> for the characterization of an energy storage device.

Charge storage ability per unit mass: Gravimetric capacitance [F g<sup>-1</sup>],

$$C_m = \frac{A}{2smV} \quad (3)$$

Charge storage ability per unit area: Areal capacitance [F cm<sup>-2</sup>],

$$C_A = \frac{A}{2saV} \quad (4)$$

Amount of energy able to deliver: Energy density [Wh kg<sup>-1</sup>],

$$E = \frac{1}{2} CV^2 \quad (5)$$

How faster is the energy to deliver: Power density [W kg<sup>-1</sup>],

$$P = \frac{E}{t} \quad (6)$$

where,  $C$  = capacitance,  $V$  = voltage window,  $t$  = discharge time,  $A$  = integrated area of the CV curve,  $s$  = scan rate (mV s<sup>-1</sup>),  $m$  = mass of the electroactive material on both electrodes, and  $a$  = area of the electrode.

**Heating Properties of the Coated Fabric:** The electro-thermal behavior of coated glass fiber fabric was measured using a thermal camera (TIM640, Micro-Epsilon, Germany) and a power supply unit (Stabilized Power Supply L 30D, Farnell Instruments LTD, UK) which supplies different voltages ranging from 5, 7, 10, and 15 V and the current was noted

from the power supply unit. The coated glass fiber fabrics were placed over the device plate. The thermal camera was installed on a tripod and connected to the computer. The thermal images obtained by the camera were extracted on the computer through the device software (TIM Connect). The changes in temperature of the coated glass fabric and achieved current were observed and recorded at various supplied voltages.

**Strain Sensitivity of the Coated Glass Fiber Fabric:** 2D materials coated glass fiber fabrics were also tested for strain sensitivity. The samples were held between the caliper’s external jaws by two large metal clips (Testometric Tensile Tester, load cell 100 kgf) hooked up to a multimeter. The multimeter monitored the relative change in the electrical resistance while stretching the fabric sensor. The voltmeter’s voltage was set to 1.0 V. Stretch and recovery tests of the fabrics were performed using five specimens (70mm × 25mm) of each set of untreated and graphene/MoS<sub>2</sub> coated fabrics. The fabric stretch ratio or strain (%) denoted as  $\epsilon$  was calculated using the following formula.

$$\text{Strain (\%)}, \epsilon = \frac{L - L_0}{L_0} \times 100 \quad (7)$$

where  $L_0$  is the initial gauge length of testing specimen while  $L$  is the length of testing specimen under loading.

**Manufacturing of Multifunctional Smart Composite Structure:** Multifunctional smart composite was manufactured using a VARI.<sup>[11]</sup> The process employed room temperature-curable biobased laminating epoxy resin and biobased laminating hardener.<sup>[87]</sup> The slow-curing bio-hardener and bio-epoxy resin were mixed at a ratio of 100:43. 10 g of PVA-H<sub>2</sub>SO<sub>4</sub> gel electrolyte was then mixed with an amount of 200 g of epoxy-hardener mixture to achieve the best balance of electrochemical and mechanical performance. Then, with a weight-to-epoxy-hardener ratio of 5%, a piece of glass fiber fabric was immersed in PVA-H<sub>2</sub>SO<sub>4</sub> gel electrolyte. Untreated glass fiber fabric was positioned against a backplate made of a smooth metal sheet; electrolyte-coated glass fiber fabric was sandwiched between the graphene/MoS<sub>2</sub> coated fabrics to act as separators and electrodes, respectively. Over the top electrode, a second absorbent layer of untreated glass fiber fabric was subjected. The surface of each electrode contains a connecting wire attached to it. Prior to that, untreated and treated glass fabrics were then dried in an oven at 50 °C for 15 min to ensure there was no moisture left in the fibers. To de-mold the resin-infused composite from the metal base plate, a peel ply was used. A mesh fabric was additionally used to guarantee an even flow of resin during the infusion procedure. Finally, a nylon plastic bag was used to completely seal the arrangement, ensuring a negative atmospheric pressure inside the bag by switching on the vacuum pump. To avoid the presence of any air bubbles, the resin was de-gassed twice; for 30 min before and for 10 min after mixing with the hardener and electrolyte as the pot life was only 43 min. By marking the resin level in the resin reservoir and continually monitoring the change in level over time, the resin was then infused into the bag using an inlet pipe while keeping a consistent flow. To ensure that composites were fully cured, infused preforms were kept at room temperature for 24 h inside the bag.

## Supporting Information

Supporting Information is available from the Wiley Online Library or from the author.

## Acknowledgements

The authors gratefully acknowledge funding from the Commonwealth Scholarship Commission (CSC) UK for a Ph.D. scholarship for M.D., and UKRI Research England the Expanding Excellence in England (E3) grant. The authors also acknowledge scientific illustration support from Natalie Corner. KSN acknowledges support from the Ministry of Education, Singapore (Research Centre of Excellence award to the Institute for Functional

Intelligent Materials, I-FIM, project No. EDUNC-33-18-279-V12) and from the Royal Society (UK, grant number RSR/R\190000).

## Conflict of Interest

The authors declare no conflict of interest.

## Data Availability Statement

The data that support the findings of this study are available from the corresponding author upon reasonable request.

## Keywords

2D materials, energy storage devices, fiber reinforced composites, heating elements, heterostructures, multifunctional smart composites, structural health monitoring

Received: May 30, 2023

Revised: July 13, 2023

Published online:

- [1] M. H. Islam, S. Afroj, M. A. Uddin, D. V. Andreeva, K. S. Novoselov, N. Karim, *Adv. Funct. Mater.* **2022**, *32*, 2205723.
- [2] X. Yu, H. Cheng, M. Zhang, Y. Zhao, L. Qu, G. Shi, *Nat. Rev. Mater.* **2017**, *2*, 17046.
- [3] R. F. Gibson, *Compos. Struct.* **2010**, *92*, 2793.
- [4] N. Yamamoto, R. G. de Villoria, B. L. Wardle, *Compos. Sci. Technol.* **2012**, *72*, 2009.
- [5] A. Mirabedini, A. Ang, M. Nikzad, B. Fox, K.-T. Lau, N. Hameed, *Adv. Sci.* **2020**, *7*, 1903501.
- [6] E. García-Macías, A. D'Alessandro, R. Castro-Triguero, D. Pérez-Mira, F. Ubertini, *Compos. Struct.* **2017**, *163*, 195.
- [7] H. Asanuma, *JOM* **2000**, *52*, 21.
- [8] K. Chu, S.-C. Lee, S. Lee, D. Kim, C. Moon, S.-H. Park, *Nanoscale* **2015**, *7*, 471.
- [9] S. Araby, Q. Meng, L. Zhang, I. Zaman, P. Majewski, J. Ma, *Nanotechnology* **2015**, *26*, 112001.
- [10] C. Liao, Y. Li, S. C. Tjong, *Int. J. Mol. Sci.* **2018**, *19*, 3564.
- [11] N. Karim, F. Sarker, S. Afroj, M. Zhang, P. Potluri, K. S. Novoselov, *Adv. Sustainable Syst.* **2021**, *5*, 2000228.
- [12] Y. Lei, T. Zhang, Y.-C. Lin, T. Granzier-Nakajima, G. Bepete, D. A. Kowalczyk, Z. Lin, D. Zhou, T. F. Schranhamer, A. Dodda, A. Sebastian, Y. Chen, Y. Liu, G. Pourtois, T. J. Kempa, B. Schuler, M. T. Edmonds, S. Y. Quek, U. Wurstbauer, S. M. Wu, N. R. Glavin, S. Das, S. P. Dash, J. M. Redwing, J. A. Robinson, M. Terrones, *ACS Nanosci. Au* **2022**, *2*, 450.
- [13] K. S. Novoselov, A. Mishchenko, A. Carvalho, A. H. C. Neto, *Science* **2016**, *353*, aac9439.
- [14] J. J. Park, W. J. Hyun, S. C. Mun, Y. T. Park, O. O. Park, *ACS Appl. Mater. Interfaces* **2015**, *7*, 6317.
- [15] S. Afroj, L. Britnell, T. Hasan, D. V. Andreeva, K. S. Novoselov, N. Karim, *Adv. Funct. Mater.* **2021**, *31*, 2107407.
- [16] Y. Wang, Y. Wang, Y. Yang, *Adv. Energy Mater.* **2018**, *8*, 1800961.
- [17] C. Yan, J. Wang, W. Kang, M. Cui, X. Wang, C. Y. Foo, K. J. Chee, P. S. Lee, *Adv. Mater.* **2014**, *26*, 2022.
- [18] M. R. Islam, S. Afroj, C. Beach, M. Islam, C. Parraman, A. Abdelkader, A. Casson, K. Novoselov, N. Karim, *iScience* **2022**, *25*, 103945.
- [19] M. Dulal, S. Afroj, J. Ahn, Y. Cho, C. Carr, I.-D. Kim, N. Karim, *ACS Nano* **2022**, *16*, 19755.
- [20] F. Sarker, P. Potluri, S. Afroj, V. Koncherry, K. S. Novoselov, N. Karim, *ACS Appl. Mater. Interfaces* **2019**, *11*, 21166.
- [21] S. Tan, S. Afroj, D. Li, M. R. Islam, J. Wu, G. Cai, N. Karim, Z. Zhao, *iScience* **2023**, *26*, 106403.
- [22] N. Karim, S. Afroj, A. Malandraki, S. Butterworth, C. Beach, M. Rigout, K. Novoselov, A. Casson, S. Yeates, *J. Mater. Chem. C* **2017**, *5*, 11640.
- [23] M. A. Uddin, S. Afroj, T. Hasan, C. Carr, K. S. Novoselov, N. Karim, *Adv. Sustainable Syst.* **2022**, *6*, 2100176.
- [24] S. Maiti, M. R. Islam, M. A. Uddin, S. Afroj, S. J. Eichhorn, N. Karim, *Adv. Sustainable Syst.* **2022**, *6*, 2200258.
- [25] N. Karim, S. Afroj, K. Lloyd, L. C. Oaten, D. V. Andreeva, C. Carr, A. D. Farmery, I.-D. Kim, K. S. Novoselov, *ACS Nano* **2020**, *14*, 12313.
- [26] M. F. El-Kady, V. Strong, S. Dubin, R. B. Kaner, *Science* **2012**, *335*, 1326.
- [27] S. Lin, W. Feng, X. Miao, X. Zhang, S. Chen, Y. Chen, W. Wang, Y. Zhang, *Biosens. Bioelectron.* **2018**, *110*, 89.
- [28] S. Tan, M. R. Islam, H. Li, A. Fernando, S. Afroj, N. Karim, *Adv. Sens. Res.* **2022**, *1*, 2200010.
- [29] R. Rahimi, M. Ochoa, W. Yu, B. Ziaie, *ACS Appl. Mater. Interfaces* **2015**, *7*, 4463.
- [30] L.-Q. Tao, H. Tian, Y. Liu, Z.-Y. Ju, Y. Pang, Y.-Q. Chen, D.-Y. Wang, X.-G. Tian, J.-C. Yan, N.-Q. Deng, Y. Yang, T.-L. Ren, *Nat. Commun.* **2017**, *8*, 14579.
- [31] M. Saraf, K. Natarajan, S. M. Mobin, *ACS Appl. Mater. Interfaces* **2018**, *10*, 16588.
- [32] F. Clerici, M. Fontana, S. Bianco, M. Serrapede, F. Perrucci, S. Ferrero, E. Tresso, A. Lamberti, *ACS Appl. Mater. Interfaces* **2016**, *8*, 10459.
- [33] K. Chang, W. Chen, *ACS Nano* **2011**, *5*, 4720.
- [34] S. Bertolazzi, J. Brivio, A. Kis, *ACS Nano* **2011**, *5*, 9703.
- [35] J.-W. Jiang, *Front. Phys.* **2015**, *10*, 287.
- [36] L. Britnell, R. M. Ribeiro, A. Eckmann, R. Jalil, B. D. Belle, A. Mishchenko, Y.-J. Kim, R. V. Gorbachev, T. Georgiou, S. V. Morozov, A. N. Grigorenko, A. K. Geim, C. Casiraghi, A. H. C. Neto, K. S. Novoselov, *Science* **2013**, *340*, 1311.
- [37] R. Zan, Q. M. Ramasse, R. Jalil, T. Georgiou, U. Bangert, K. S. Novoselov, *ACS Nano* **2013**, *7*, 10167.
- [38] K. Roy, M. Padmanabhan, S. Goswami, T. P. Sai, S. Kaushal, A. Ghosh, *Solid State Commun.* **2013**, *175–176*, 35.
- [39] G. Algara-Siller, S. Kurasch, M. Sedighi, O. Lehtinen, U. Kaiser, *Appl. Phys. Lett.* **2013**, *103*, 203107.
- [40] N. Myoung, K. Seo, S. J. Lee, G. Ihm, *ACS Nano* **2013**, *7*, 7021.
- [41] S. K. Chakraborty, B. Kundu, B. Nayak, S. P. Dash, P. K. Sahoo, *iScience* **2022**, *25*, 103942.
- [42] O. A. Moses, L. Gao, H. Zhao, Z. Wang, M. L. Adam, Z. Sun, K. Liu, J. Wang, Y. Lu, Z. Yin, X. Yu, *Mater. Today* **2021**, *50*, 116.
- [43] Y. Xue, Y. Zhang, Y. Liu, H. Liu, J. Song, J. Sophia, J. Liu, Z. Xu, Q. Xu, Z. Wang, *ACS Nano* **2016**, *10*, 573.
- [44] W. Deng, Y. Chen, C. You, B. Liu, Y. Yang, G. Shen, S. Li, L. Sun, Y. Zhang, H. Yan, *Adv. Electron. Mater.* **2018**, *4*, 1800069.
- [45] U. Sundararaju, M. A. S. M. Haniff, P. J. Ker, P. S. Menon, *Materials* **2021**, *14*, 1672.
- [46] J. Mei, T. Liao, Z. Sun, *Energy Environ. Mater.* **2021**, *5*, 115.
- [47] R. Janeliukstis, D. Mironovs, *Mech. Compos. Mater.* **2021**, *57*, 131.
- [48] S. Afroj, N. Karim, Z. Wang, S. Tan, P. He, M. Holwill, D. Ghazaryan, A. Fernando, K. S. Novoselov, *ACS Nano* **2019**, *13*, 3847.
- [49] N. Karim, S. Afroj, S. Tan, P. He, A. Fernando, C. Carr, K. S. Novoselov, *ACS Nano* **2017**, *11*, 12266.
- [50] Q. Fang, M. Li, X. Zhao, L. Yuan, B. Wang, C. Xia, F. Ma, *Mater. Adv.* **2022**, *3*, 624.
- [51] C. Lee, X. Wei, J. W. Kysar, J. Hone, *Science* **2008**, *321*, 385.
- [52] S. Afroj, S. Tan, A. M. Abdelkader, K. S. Novoselov, N. Karim, *Adv. Funct. Mater.* **2020**, *30*, 2000293.

- [53] L. Song, T. Wang, W. Jing, X. Xie, P. Du, J. Xiong, *Mater. Res. Bull.* **2019**, *118*, 110522.
- [54] D. H. Jeon, *Energy Storage Mater.* **2019**, *18*, 139.
- [55] J. Wang, Z. Wu, K. Hu, X. Chen, H. Yin, *J. Alloys Compd.* **2015**, *619*, 38.
- [56] X. Chen, R. Paul, L. Dai, *Natl. Sci. Rev.* **2017**, *4*, 453.
- [57] A. Shameem, P. Devendran, V. Siva, R. Packiaraj, N. Nallamuthu, S. A. Bahadur, *J. Mater. Sci.: Mater. Electron.* **2019**, *30*, 3305.
- [58] T. Kim, W. Choi, H.-C. Shin, J.-Y. Choi, J. M. Kim, M.-S. Park, W.-S. Yoon, *J. Electrochem. Sci. Technol.* **2020**, *11*, 14.
- [59] W. Xiao, W. Zhou, T. Feng, Y. Zhang, H. Liu, L. Tian, *Materials* **2016**, *9*, 783.
- [60] K.-J. Huang, L. Wang, Y.-J. Liu, Y.-M. Liu, H.-B. Wang, T. Gan, L.-L. Wang, *Int. J. Hydrogen Energy* **2013**, *38*, 14027.
- [61] S. Patil, A. Harle, S. Sathaye, K. Patil, *CrystEngComm* **2014**, *16*, 10845.
- [62] D. Vikraman, K. Karuppasamy, S. Hussain, A. Kathalingam, A. Sanmugam, J. Jung, H.-S. Kim, *Composites, Part B* **2019**, *161*, 555.
- [63] R. Zhou, C.-j. Han, X.-m. Wang, *J. Power Sources* **2017**, *352*, 99.
- [64] N. H. A. Rosli, K. S. Lau, T. Winie, S. X. Chin, S. Zakaria, C. H. Chia, *J. Energy Storage* **2022**, *52*, 104991.
- [65] M. Fu, Z. Zhu, W. Chen, H. Yu, Q. Liu, *J. Mater. Sci.* **2020**, *55*, 16385.
- [66] A. Hussain, M. Malik, T. Salahuddin, S. Bilal, M. Awais, *J. Mol. Liq.* **2017**, *231*, 341.
- [67] J. Tabor, K. Chatterjee, T. K. Ghosh, *Adv. Mater. Technol.* **2020**, *5*, 1901155.
- [68] M. H. Islam, M. R. Islam, M. Dulal, S. Afroj, N. Karim, *iScience* **2022**, *25*, 103597.
- [69] P. Yang, S. Ghosh, T. Xia, J. Wang, M. A. Bissett, I. A. Kinloch, S. Barg, *Compos. Sci. Technol.* **2022**, *218*, 109199.
- [70] N. Karim, M. Zhang, S. Afroj, V. Koncherry, P. Potluri, K. S. Novoselov, *RSC Adv.* **2018**, *8*, 16815.
- [71] S. Upama, A. Mikhalchan, L. Arévalo, M. Rana, A. Pendashteh, M. J. Green, J. J. Vilatela, *ACS Appl. Mater. Interfaces* **2023**, *15*, 5590.
- [72] M. O. Faruk, A. Ahmed, M. A. Jalil, M. T. Islam, A. M. Shamim, B. Adak, M. M. Hossain, S. Mukhopadhyay, *Appl. Mater. Today* **2021**, *23*, 101025.
- [73] Y. Ma, N. Liu, L. Li, X. Hu, Z. Zou, J. Wang, S. Luo, Y. Gao, *Nat. Commun.* **2017**, *8*, 1207.
- [74] H. Zhang, D. Liu, J.-H. Lee, H. Chen, E. Kim, X. Shen, Q. Zheng, J. Yang, J.-K. Kim, *Nano-Micro Lett.* **2021**, *13*, 122.
- [75] A. Chhetry, M. Sharifuzzaman, H. Yoon, S. Sharma, X. Xuan, J. Y. Park, *ACS Appl. Mater. Interfaces* **2019**, *11*, 22531.
- [76] W. Zhang, S. Piao, L. Lin, Y. Yin, J. Guo, Z. Jiang, Y. Cho, R. Li, J. Gao, H. Pang, Y. Piao, *Chem. Eng. J.* **2022**, *435*, 135068.
- [77] F. S. Irani, A. H. Shafaghi, M. C. Tasdelen, T. Delipinar, C. E. Kaya, G. G. Yapici, M. K. Yapici, *Micromachines* **2022**, *13*, 119.
- [78] H. Qian, A. R. Kucernak, E. S. Greenhalgh, A. Bismarck, M. S. P. Shaffer, *ACS Appl. Mater. Interfaces* **2013**, *5*, 6113.
- [79] E. Senokos, Y. Ou, J. J. Torres, F. Sket, C. González, R. Marcilla, J. J. Vilatela, *Sci. Rep.* **2018**, *8*, 3407.
- [80] C. Meng, N. Muralidharan, E. Teblum, K. E. Moyer, G. D. Nessim, C. L. Pint, *Nano Lett.* **2018**, *18*, 7761.
- [81] A. Thakur, X. Dong, *Manuf. Lett.* **2020**, *24*, 1.
- [82] K. Moyer, C. Meng, B. Marshall, O. Assal, J. Eaves, D. Perez, R. Karkkainen, L. Roberson, C. L. Pint, *Energy Storage Mater.* **2020**, *24*, 676.
- [83] P. Liu, E. Sherman, A. Jacobsen, *J. Power Sources* **2009**, *189*, 646.
- [84] X. Peng, L. Peng, C. Wu, Y. Xie, *Chem. Soc. Rev.* **2014**, *43*, 3303.
- [85] A. M. Abdelkader, N. Karim, C. Vallés, S. Afroj, K. S. Novoselov, S. G. Yeates, *2D Mater.* **2017**, *4*, 035016.
- [86] M. R. Islam, S. Afroj, K. S. Novoselov, N. Karim, *Adv. Sci.* **2022**, *9*, 2203856.
- [87] M. Islam, S. Afroj, N. Karim, *ChemRxiv* **2023**.